Icarus 382 (2022) 115019

Contents lists available at ScienceDirect

Icarus

journal homepage: www.elsevier.com/locate/icarus

Research Paper

Control of the oscillations of the Martian Northern Hemisphere polar vortex by the Hadley cell and topographic forcing

Márton Mester

Department of Mathematics, University College London, London, United Kingdom

ARTICLE INFO

Keywords:
Mars, atmosphere
Mars, climate
Mars, polar caps
Atmosphere, dynamics

ABSTRACT

The oscillations of the Martian Northern Hemisphere polar vortex are examined by using the Kida vortex model to interpret the dynamics of the vortex in reanalysis data. The vortex nutating around a fixed angle with little variability in its aspect ratio is shown to be controlled by the Hadley cell and wavenumber-2 planetary-scale waves that are characterised with a stationary component that is shown to be linked directly to Martian topography. The wave forcing and the Hadley cell structure are modelled as a strain and a rotational flow in Kida's model. It is shown that the strain and rotational flow are strongly negatively correlated, acting against vortex elongation in Kida's model. The result suggests that periods of high topographic forcing events are accompanied with a weakening in the Hadley cell winds and thus provides an explanation why vortex splits are rare on Mars.

1. Introduction

A dominant structure of the atmosphere at Mars' winter hemisphere is its polar vortex, a low temperature region located above the pole, surrounded by strong westerly winds, and often compared to stratospheric polar vortices on Earth due to its similar spatial extent (Mitchell et al., 2015). However, the Martian polar vortex forms on the poleward side of the descending branch of the Hadley cell, and changes in the Hadley circulation directly influence the vortex, which suggests that Martian polar vortices can also be compared to tropospheric polar vortices on Earth (Waugh et al., 2016). The atmosphere of Mars is mainly composed of CO_2, which condenses over the winter pole forming dry ice on the surface. The associated latent heat release acts as a potential vorticity (PV) sink (Toigo et al., 2017) above the pole, manifesting in a PV structure that has a local minimum above the pole surrounded by patches of high PV, caused by inhomogeneous deposition of CO_2 (Rostami et al., 2018). This structure is commonly referred to as an annular vortex, since the time-averaged PV field shows an annular vortex shape (Barnes and Haberle, 1996; Mitchell et al., 2015). Despite the annular structure, the vortex is well-described as a region of elevated PV, and idealised model studies (Scott et al., 2020) show that this PV structure forms naturally from the combination of an angular momentum conserving Hadley cell driven by off-equatorial heating, and a heating source associated with latent heat release over the polar regions.

At both hemispheres, the Martian polar vortices are seen to be aligned with and nutate around a fixed angle in reanalysis data (Mitchell et al., 2015), as opposed to stratospheric polar vortices on Earth, where, in addition to a stationary wavenumber-2 wave, an eastward propagating wavenumber-2 wave is present on the vortex edge (on both hemispheres), resulting in an anticlockwise rotating vortex on the Northern, and clockwise rotating vortex on the Southern Hemisphere.

While stratospheric polar vortices (on Earth) undergo consistent filamentation, with the detached filaments quickly mixing in the surrounding surf zone, reanalysis data shows no filamentation in the case of Martian polar vortices (Mitchell et al., 2015), at least on the 350 K isentropic level. A possible explanation for the lack of filamentation is the resolution of the MACDA reanalysis; however, similar resolutions on Earth still exhibit filamentation (Mitchell et al., 2015). Since detached filaments can transport polar air to the Hadley cell, their (non-)existence may contribute to trace gas distributions and the water cycle on Mars.

Recent studies that discuss the role of the topography and the Hadley cell in the dynamics of Mars' polar vortex have focused on capturing the time-averaged PV structure of the vortex, which is (at a given isentropic level) an annular, near elliptical shape aligned at a fixed orientation with respect to topography (Mitchell et al., 2015). In particular, Seviour et al. (2017) illustrated by the use of a rotating shallow-water model that the time-averaged polar vortex profile can be recovered when a wavenumber-2 forcing of sufficient amplitude is introduced along with thermal relaxation. The variability of the time-averaged vortex is illustrated by idealised model studies (Ball et al., 2021) to be governed by an interplay of topographic forcing and a

E-mail address: marton.mester.16@ucl.ac.uk.

https://doi.org/10.1016/j.icarus.2022.115019
Received 6 October 2021; Received in revised form 24 March 2022; Accepted 30 March 2022
Available online 9 April 2022
0019-1035/© 2022 The Author. Published by Elsevier Inc. This is an open access article under the CC BY license (http://creativecommons.org/licenses/by/4.0/).

Hadley cell strengthened by a background dust loading, with latent heat release playing only a secondary role. Furthermore, changes in the elliptical shape of a 20-sol time-averaged vortex correlate with changes in the corresponding 20-sol time-averaged wavenumber-2 wave experienced by the vortex (Streeter et al., 2021), supporting the idea that topography is a main driver of polar vortex variability.

Like stratospheric polar vortices on Earth, the Martian polar vortex can also undergo a quick rise in temperatures, as has been observed to happen during northern winter solstice dust storms when the meridional Hadley circulation transports dust poleward and the asymmetric dust loading generates thermally forced planetary waves (Guzewich et al., 2016; Smith, 2004; Wilson, 1997). Simplified nonlinear model studies (Barnes and Hollingsworth, 1987), similar to the Holton–Mass model of terrestrial SSWs (Holton and Mass, 1976), demonstrated that the solar heated dusty Hadley circulation and the planetary wave circulation forced at surface can indeed explain polar warmings when the atmosphere is sufficiently dusty, and argued that only wavenumber-1 planetary waves are responsible for triggering the warming with the wavenumber-2 waves not being able to penetrate high enough in the atmosphere during dusty spells.

In this paper, we study how the topographic forcing and the Hadley cell controls the evolution of the nutation cycles (or oscillations) of the Martian Northern Hemisphere (NH) polar vortex in reanalysis data by applying the method of 'dynamical elliptical diagnostics' (Mester and Esler, 2020). These oscillations are called nutations when the elongated vortex shape repeatedly undergoes an anticlockwise and a clockwise motion in quick succession around a fixed orientation (longitude circle) and without making a full cycle in either clockwise or anticlockwise direction on the time scale of approximately 20 h (see Fig. 1). During a nutation cycle, the vortex orientation is therefore constrained into a range of longitude circles, and this property of the Martian NH polar vortex has been recovered in reanalysis data (Mitchell et al., 2015) in Martian Years 24–26. The consistently nutating behaviour of the Martian NH polar vortex in Martian Years 24–26 is different from the observed oscillation cycles of Earth' stratospheric polar vortices, where the nutation cycles are only occasional cases at both hemispheres (for SH, see e.g. Mester and Esler, 2020). Instead, the NH and SH polar vortices on Earth typically undergo a full anticlockwise or clockwise oscillation cycle, respectively.

The method of dynamical elliptical diagnostics models the dynamical evolution of the polar vortex as a Kida vortex (Kida, 1981), describing the motion of an elliptical patch of uniform vorticity in an unsteady linear background flow. While the Kida vortex model has its obvious limitations, describing a two-dimensional vortex in a linear background flow, whereas the polar vortex is a three-dimensional vortex in spherical geometry in a turbulent planetary atmosphere, the coherence in the elliptical structure of the Martian polar vortex in the vertical direction (Mitchell et al., 2015) suggests that a two-dimensional model can still capture the essential dynamics of the oscillations of the vortex. It should also be noted that by using the Kida vortex model, we neglect the effects of the interior dynamics (the PV sink associated to latent heat release) on the vortex oscillations, and in fact it has been argued that the variability of the Martian polar vortex is not significantly influenced by latent heat release (Ball et al., 2021). By fitting a Kida vortex to the 'observed' evolution of the vortex, our focus will be on the ellipticity and the orientation of the vortex, which is essentially the amplitude and phase of a wavenumber-2 wave on the vortex edge. The vortex is controlled by a strain and a rotational component of the background flow. It will be argued that the stationary component of the strain (wavenumber-2 forcing experienced by the vortex) can be semi-directly associated to the topography of Mars, and the rotational component is controlled by the wind structure in the Hadley cell.

Therefore, this study provides a new perspective on how the Hadley cell and the wavenumber-2 topographic forcing controls the oscillations (nutations) of the Martian NH polar vortex. In particular, we will discuss how the consistent nutation of the vortex about a fixed orientation is supported by the combination of the topographic forcing and the Hadley circulation, and our methodology will provide a new, more detailed insight on why it is not likely to observe vortex splits under typical Martian atmospheric conditions.

The paper is organised as follows. In Section 2 we describe how the dynamical elliptical diagnostics are obtained from reanalysis data and describe the underlying simple dynamical model of Kida's vortex. In Section 3, we detail the output of the dynamical elliptical diagnostics and we argue that the vortex is controlled by the Martian topography and the Hadley cell. Furthermore, we consider the conditions that are necessary for vortex splitting and argue that it is not likely to observe vortex splits on Mars. Finally, in Section 4, conclusions are drawn.

2. Dataset and methodology

The application of the dynamical elliptical diagnostics (Mester and Esler, 2020) requires the construction of a time-series of elliptical diagnostics (Waugh, 1997), the latter being a descriptor of the geometry of the polar vortex and is determined from the distribution of potential vorticity on a given isentropic level.

2.1. Derivation of the potential vorticity structure

We infer the potential vorticity structure from reanalysis data, referred to as 'reanalysis output', taken from the Mars Analysis Correction Data Assimilation (MACDA) MGS/TES v1.0 dataset (Montabone et al., 2014) for Martian Years (MYs) 24–26 and from the Open access to Mars Assimilated Remote Soundings (OpenMARS) dataset (Holmes et al., 2019) for MYs 30–32. The two datasets use the same assimilation scheme; the output of MACDA for MYs 24–26 is identical to the output of OpenMARS over the MYs 24–26 time period. While the same assimilation scheme is used for MYs 24–26 and MYs 30–32, the assimilation scheme uses observational data from the Thermal Emission Spectrometer (TES) instrument in the MYs 24–26 period, and uses observational data from the Mars Climate Sounder (MCS) instrument in the MYs 30-32 period, and thus the difference in data retrieval may lead to systematic differences beyond natural variability in the two time periods where the data used are retrieved from different instruments (see e.g. Greybush et al., 2019). The time difference between two successive reanalysis output is 2 h, and we consider the time window $240°-330°$ L_s each year, where L_s denotes solar longitudes. While the OpenMARS dataset contains reanalysis output from MYs 28–29 as well, we do not consider the output for MYs 28–29. In MY 28, a global dust storm developed shortly before northern winter solstice, resulting in a NH polar vortex that is characteristically weaker than the NH polar vortex in MYs 24–26 and 30–32, suggesting that a potential vorticity contour dynamics perspective of the Martian NH polar vortex evolution may not be applicable in MY 28. Finally, we do not consider MY 29, since there was no data retrieval between $L_s = 278°$, MY 29 and $L_s = 19°$, MY 30.

While the datasets do not include potential vorticity explicitly, they include data of surface pressure $p_{surf}(\boldsymbol{x})$, zonal $u(\boldsymbol{x},\sigma)$ and meridional $v(\boldsymbol{x},\sigma)$ wind and temperature $T(\boldsymbol{x},\sigma)$ supplied on a spherical grid with a $5° \times 5°$ resolution. The vertical levels are given by 25 and 35 atmospheric σ-coordinates for MYs 24–26 and MYs 30–32, respectively, defined by $\sigma(\boldsymbol{x},z) = p(\boldsymbol{x},z)/p_{surf}(\boldsymbol{x})$, where p is the pressure. We define the reference pressure on Mars as the average surface pressure $p_0 = 6.1$ hPa, and the potential temperature on the σ_n level is given by

$$\theta_n(\boldsymbol{x},\sigma) = T(\boldsymbol{x})\left(\frac{\sigma_n p_{surf}(\boldsymbol{x})}{p_0}\right)^{c_p/R}, \tag{1}$$

where c_p/R is the ratio of the specific heat at constant pressure and the universal gas constant, and this ratio is approximated by 4.4 on Mars following Mitchell et al. (2015), as its atmosphere is primarily

composed of carbon dioxide. Since we are interested in the dynamics on a given isentropic level, and data is supplied on 25 and 35 σ-coordinates (for MYs 24–26 and 30–32, respectively), we apply a cubic interpolation on $\theta_n(\boldsymbol{x},\sigma)$ to derive a potential temperature profile $\theta(\boldsymbol{x},\sigma)$ that is now a continuous function of σ. Now the inversion of (1) results in

$$\sigma(\boldsymbol{x},\theta) = \frac{p_0}{p_{surf}(\boldsymbol{x})}\left(\frac{\theta}{T(\boldsymbol{x})}\right)^{R/c_p}. \tag{2}$$

Next, we use a cubic interpolation on $u(\boldsymbol{x},\sigma_n)$ and $v(\boldsymbol{x},\sigma_n)$ in the vertical direction to make the velocity profile continuous in σ. The velocity profiles $u(\boldsymbol{x},\theta)$ and $v(\boldsymbol{x},\theta)$ can now be simply determined by substituting (2) in $u(\boldsymbol{x},\sigma)$ and $v(\boldsymbol{x},\sigma)$.

Ertel's potential vorticity is given by

$$q = -g(f+\zeta_\theta)\partial_p\theta, \tag{3}$$

where the gravitational constant on Mars takes the value $g = 3.711$ m s^{-2} and the Coriolis-term is given by $f = 1.42\times10^{-4}\sin\phi$ s^{-1}. The vorticity ζ_θ is calculated from the $u(\boldsymbol{x},\theta)$ and $v(\boldsymbol{x},\theta)$ fields and

$$\partial_p\theta = \partial_\sigma\theta\partial_p\sigma = \frac{1}{p_{surf}}\partial_\sigma\theta \tag{4}$$

is determined from the interpolated potential temperature field $\theta(\boldsymbol{x},\sigma)$.

2.2. Elliptical diagnostics

Elliptical diagnostics (Waugh, 1997), a commonly used technique to characterise stratospheric polar vortices on Earth, were first applied on the Martian polar vortices by Mitchell et al. (2015), who compared the climatological behaviour of Martian polar vortices to stratospheric polar vortices on Earth, using the MACDA reanalysis dataset. Similarly to their analysis, we direct our investigation of the polar vortices on the 350 K isentropic level, which corresponds to the approximately 35–40 km pseudo-altitude height at polar regions.

The method of elliptical diagnostics constructs an ellipse that is a best-fit to the geometry of the potential vorticity structure of the vortex, describing the vortex area, centroid, aspect ratio Λ and orientation Θ. For the technical details of the construction of the ellipse, the reader is referred to Appendix A.

2.2.1. Nutation cycles of the vortex

The geometry and the oscillations of the Martian polar vortex in the interval $L_s = 254.83° - 255.27°$ in MY 24 is displayed on Fig. 1, illustrating that the vortex geometry is captured very accurately by the elliptical diagnostics at all times. During this representative 16-hour interval the vortex undergoes a complete nutation cycle around a fixed angle, therefore, the period of a nutation cycle is only a few times longer than the time between two successive reanalysis output.

2.3. A non-singular, Hamiltonian formulation of Kida's model

The evolution of the aspect ratio $\Lambda \geq 1$ and the orientation Θ of an elliptical patch of uniform, constant vorticity ω in an unsteady linear background flow is given by Kida's equations (Kida, 1981),

$$\begin{aligned}\dot{\Theta} &= \Omega + \frac{\omega\Lambda}{(\Lambda+1)^2} - \frac{\Lambda^2+1}{\Lambda^2-1}\Gamma\sin(2\Theta-2\Phi)\\ \dot{\Lambda} &= 2\Lambda\Gamma\cos(2\Theta-2\Phi),\end{aligned} \tag{5}$$

where the background flow consists of a strain flow with magnitude $\Gamma(t)$ and axis aligned at angle $\Phi(t)$, and a solid body rotation $\Omega(t)$.

In this study, we consider a transformed version of Kida's equations (Melander et al., 1986; Mester and Esler, 2020), by defining a strain-rotation vector $\boldsymbol{\Gamma} \equiv (\Gamma_1,\Gamma_2,\Gamma_3)^T = (\Gamma\cos(2\phi),\Gamma\sin(2\phi),\Omega)^T$ and introducing the ellipticity vector

$$\boldsymbol{X} \equiv \begin{pmatrix} X \\ Y \end{pmatrix} = (\Lambda^{1/2}-\Lambda^{-1/2})\begin{pmatrix}\cos 2\Theta \\ \sin 2\Theta\end{pmatrix}, \tag{6}$$

where the magnitude $|\boldsymbol{X}|$ of the ellipticity vector and the aspect ratio Λ are in a monotonic relationship, given by

$$\Lambda = \frac{1}{4}\left(|\boldsymbol{X}| + \left(|\boldsymbol{X}|^2+4\right)^{1/2}\right)^2. \tag{7}$$

Using the transformation given by (6), Kida's equations (5) can be recast in the form of Hamilton's equations

$$\dot{\boldsymbol{X}} = \nabla^\perp H, \tag{8}$$

where $\nabla^\perp \equiv \boldsymbol{k}\times\nabla$ is the skew-gradient operator with respect to $\boldsymbol{X}$, where the Hamiltonian H of the system is given by

$$H(\boldsymbol{X}) = \left(|\boldsymbol{X}|^2+4\right)^{1/2}\boldsymbol{\Gamma}\cdot\left(\boldsymbol{k}\times\boldsymbol{X}\right) + |\boldsymbol{X}|^2\,\boldsymbol{\Gamma}\cdot\boldsymbol{k} + \omega\log\left(\frac{|\boldsymbol{X}|^2+4}{4}\right). \tag{9}$$

The transformed system (8)–(9) has two key properties that makes it more advantageous than the original equations given by (5). First, the singularity at $\Lambda = 1$ in (5) is removed and in the transformed system a circular vortex corresponds to $\boldsymbol{X} = 0$. Second, the Hamiltonian structure allows a phase-portrait interpretation of the dynamics, which we will use to interpret the vortex oscillations in Section 3.

2.4. Dynamical elliptical diagnostics

The method of dynamical elliptical diagnostics interpret the evolution of the elliptical diagnostics (from reanalysis output) as a Kida vortex in an unsteady background flow by calculating the minimiser of the functional

$$J(\boldsymbol{\Gamma},\boldsymbol{X},\boldsymbol{\mu}) = \int_0^T \left(|\dot{\boldsymbol{\Gamma}}|^2 + \epsilon^2|\boldsymbol{X}-\boldsymbol{X}_{re}(t)|^2 + \boldsymbol{\mu}\cdot(\dot{\boldsymbol{X}}-\nabla^\perp H)\right)\mathrm{d}t, \tag{10}$$

where $\epsilon^2 = 0.01$ is a parameter controlling the smoothness of the solution and takes the same value (motivated by testing different values of ϵ, not shown) as in Mester and Esler (2020), and the 'reanalysis' ellipticity vector is determined from reanalysis output, using elliptical diagnostics, given by

$$\boldsymbol{X}_{re} = (X_{re},Y_{re})^T = (\Lambda^{1/2}-\Lambda^{-1/2})(\cos 2\Theta,\sin 2\Theta)^T. \tag{11}$$

The term $(\dot{\boldsymbol{X}}-\nabla^\perp H)$ is simply Kida's equation in ellipticity variables (8) when it is set to zero (i.e. $\dot{\boldsymbol{X}} = \nabla^\perp H$), and $\nabla^\perp H$ is a function $\nabla^\perp H(\boldsymbol{X},\boldsymbol{\Gamma},\omega)$, where ω is a constant parameter, a descriptor of the vorticity jump at the edge of the polar vortex.

By calculating the difference between the average vorticity inside the vortex and the average vorticity in the region bounded by the vortex boundary and the 32.5° latitude circle, we find that $2.45 - 2.50\times10^{-4}$ s^{-1} is a good estimator of the vorticity jump. We nondimensionalise by defining 2 Martian hours (1 Mars hour = 1.0275 Earth hours) to be a time unit, since MACDA provides data every 2 h. The time between two successive reanalysis output is $\Delta t \approx 7400$ s. Hence, the non-dimensional vorticity jump is $\approx 1.81 - 1.85$ which we approximate by $\omega = 1.83$.

The optimisation problem is solved by the use of standard techniques of variational calculus, for details the reader is referred to Appendix B. The solution (or output) of the optimisation problem (10) includes the time series of an assimilated ellipticity vector $\boldsymbol{X}$ and a strain-rotation vector $\boldsymbol{\Gamma} = (\Gamma_1,\Gamma_2,\Gamma_3)^T/\omega$ with two strain components forming the strain vector $\boldsymbol{\Gamma}_H/\omega = (\Gamma_1,\Gamma_2)^T/\omega$, and a rotation component Γ_3/ω. The time-series of the ellipticity and strain rotation vectors $\boldsymbol{X},\boldsymbol{\Gamma}$ are referred to as the dynamical elliptical diagnostics of the polar vortex, and forms the basis of this study.

3. Results

The evolution of the polar vortex is investigated between the 240° – 330° solar longitudes for Martian Years 24–26 and 30–32. The time-interval is chosen so that the mid- and late-winter evolution of the vortex is considered, which includes winter solstice at $L_s = 270°$, but does not include spring equinox at $L_s = 360°$, and this time window is characterised by a strong, coherent polar vortex (Mitchell et al., 2015), where the methods of potential vorticity based contour dynamics, and Kida's model is appropriate.

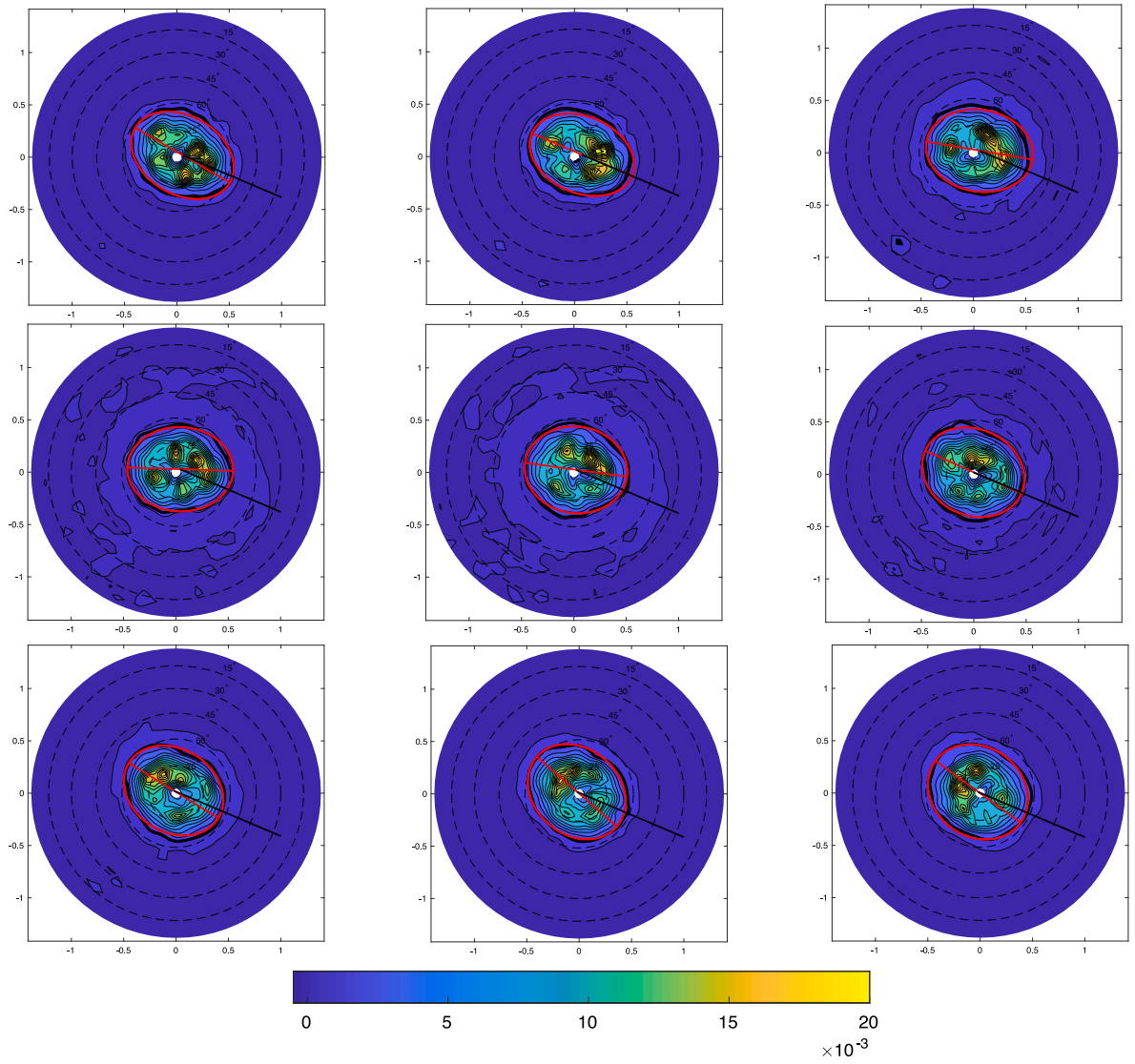


Fig. 1. The nutations of the Martian Northern Hemisphere polar vortex between $L_s = 254.83° - 255.27°$ in MY 24 on the 350 K isentropic level. Snapshots show the potential vorticity structure (units are in km^2 kg^{-1} s^{-1}) of the vortex every 2 Martian hours. The vortex boundary is shown as a black contour and the elliptical fit and its main axis is shown in red. Black line shows the direction of the climatological mean of the orientation of the vortex, aligned approximately with the -23° longitude circle. The axes are given by the Cartesian coordinates under Lambert's projection, scaled by the radius of Mars (under this projection and scaling, the equator is located at radius $\sqrt{2}$). (For interpretation of the references to colour in this figure legend, the reader is referred to the web version of this article.)

3.1. Behaviour of the strain-rotation vector

The assimilation reveals that the underlying strain field $\boldsymbol{\Gamma}_H/\omega$ has a strongly preferred direction during the entire winter season (see Fig. 2) in each of the Martian Years we investigated. Its magnitude follows different patterns in MYs 24–26 and MYs 30–32. In MYs 24–26, the strain magnitude experiences a slight strengthening between approximately $L_s = 240°$ and $L_s = 290°$ and then a subsequent weakening late winter (see Fig. 3). In MYs 30–32, the opposite trend can be noticed, a slight decrease in strain magnitude is followed by a more prominent strengthening late winter.

The rotational component experiences large oscillations within a winter season in MYs 24–26, covering the (−0.15,-0.05) regime with 'climatological mean' value -0.1031 during years MYs 24–26 and becoming more negative late winter. In contrast, the rotational component covers the more negative range (−0.18,-0.8) with 'climatological mean' value -0.1364 during years MYs 30–32 (see Fig. 4) and becomes less negative late winter in years MY 30–31. Therefore, while there is consistency within each of the two three-year-long period, the two periods themselves follow different trends with respect to their strain-rotation vector.

A phase-portrait representation (Fig. 5, left panel) shows that a strain-rotation vector $\boldsymbol{\Gamma}_m/\omega$, which is the stationary part of the obtained strain-rotation vector during the $L_s = 240° - 330°$ period in MYs 24–26, can capture the evolution of the polar vortex quite well, with orbits cycling around a fixed point and filling the entire nutation (NUT) regime. The phase-portrait representation shows constant lines of the Hamiltonian H of Kida's system given by Eq. (9) for the strain-rotation vector $\boldsymbol{\Gamma}_m/\omega$. If the strain-rotation vector was constant in time, the vortex state would move along a single Hamiltonian line, as H is conserved by the motions of Kida's vortex. While the strain-rotation vector is time-dependent, this representation, using the stationary part during the MYs 24–26 period, still describes the qualitatively different regimes of behaviour of the vortex, typical to MYs 24–26. The rate of change of the ellipticity vector, given by Eq. (8), is visualised using arrows (Fig. 5), showing the direction of the motion under the assumption of fixed, time-independent strain-rotation vector $\boldsymbol{\Gamma}_m/\omega$. This representation reveals a NUT regime that is characterised by

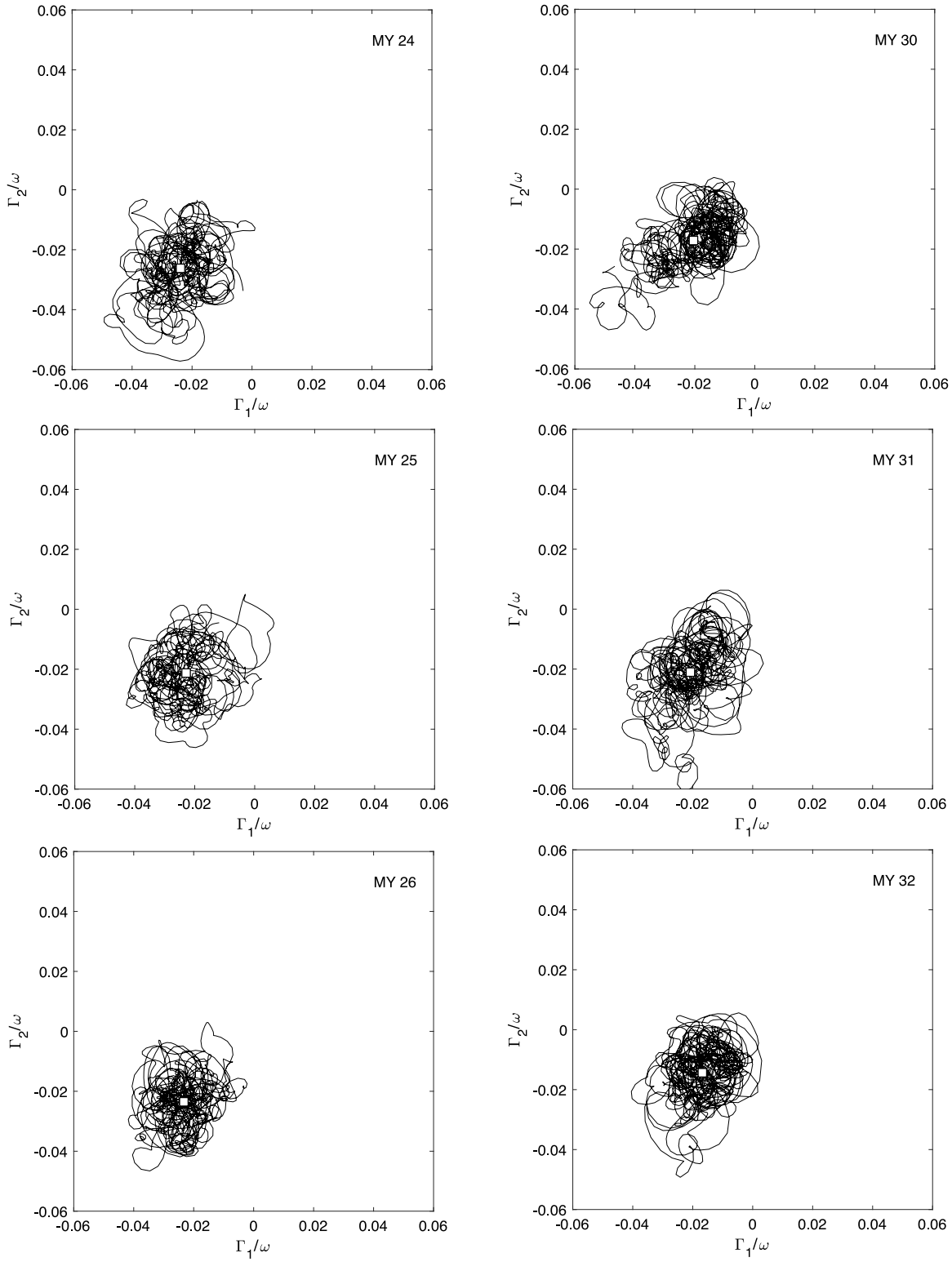


Fig. 2. The evolution of the strain components during the $L_s = 240° - 330°$ period in Martian Years 24–26 (left) and Martian Years 30–32 (right). White squares show the location of the seasonal mean value of the strain vector.

low amplitude motion with both clockwise and anticlockwise phases (i.e. motions here can be described as nutating around a fixed angle). A number of different types of accessible Hamiltonian cycles are revealed, and can be characterised relative to the self-intersecting separatrix, which itself is a Hamiltonian line passing through a saddle point of Kida's vortex system. Inside of the small loop of the separatrix, one can find a regime where the vortex undergoes low amplitude, anticlockwise motion (ACW regime). The small loop is surrounded by a much larger, oscillating (OSC) regime, where the vortex undergoes both a very large amplitude clockwise and relatively large amplitude anticlockwise motion. The OSC regime is surrounded by a regime characterised by very large amplitude, clockwise oscillations (CW).

While the vortex is well constrained within the NUT regime for MYs 24–26, it also undergoes periodic, low-amplitude, anticlockwise

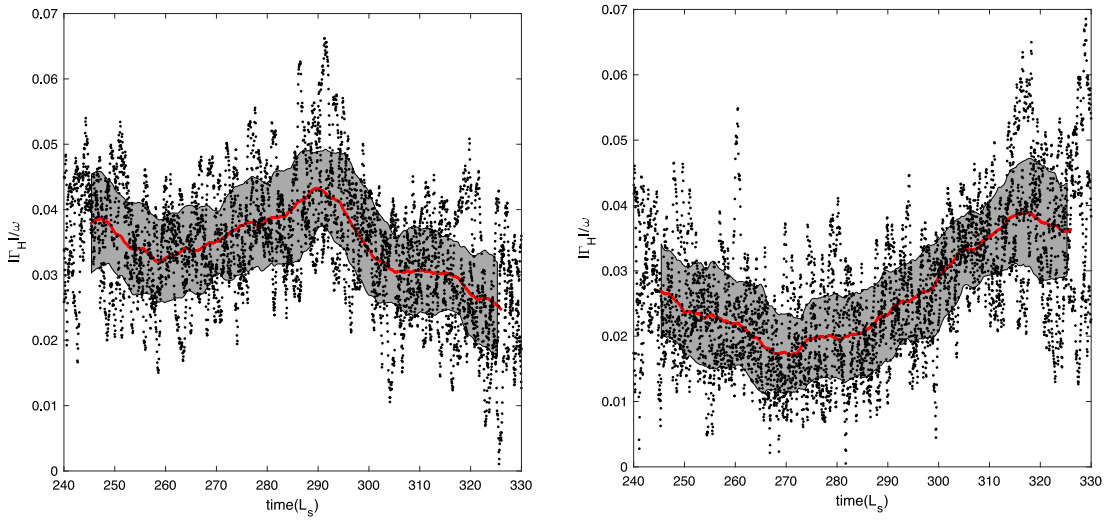


Fig. 3. The seasonal cycle of the magnitude of the strain component during the $L_s = 240° - 330°$ periods in Martian Years 24–26 (left) and Martian Years 30–32 (right). The red line and the shaded area shows the 10-sol mean and standard deviation. (For interpretation of the references to colour in this figure legend, the reader is referred to the web version of this article.)

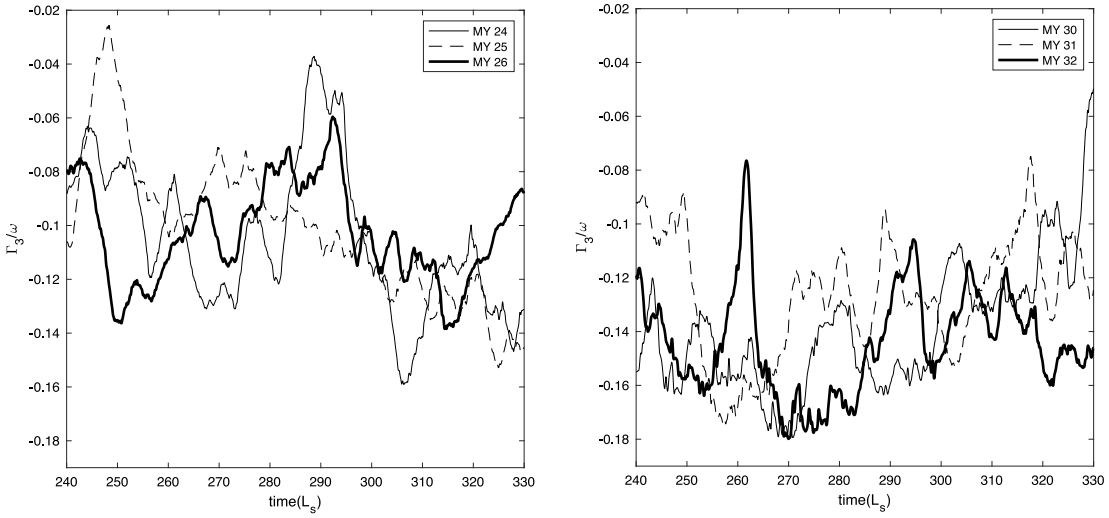


Fig. 4. The evolution of the rotational component during the $L_s = 240° - 330°$ periods in Martian Years 24–26(left) and Martian Years 30–32 (right).

(ACW) oscillation cycles in MYs 30–32 (Fig. 6), when the rotational component is more negative compared to MYs 24–26, resulting in a smaller NUT regime. However, as the more negative values of the rotation component are accompanied with weaker strain, the vortex stays well inside the ACW region without approaching the separatrix.

3.2. Vortex split characterisation

In Kida's model, rapid rises in ellipticity (i.e. in wavenumber-2 wave amplitude) occur when the vortex crosses the separatrix, i.e. it leaves the NUT and ACW regimes and enters the OSC regime, and such transitions have been associated with resonantly excited vortex splitting stratospheric sudden warmings on Earth (Esler and Mester, 2019; Matthewman and Esler, 2011; Mester and Esler, 2020; Plumb, 1981). It appears that in the six Martian Years investigated, the ellipticity variables never approached the separatrix that corresponds to typical Martian conditions.

It should be kept in mind that Γ_3/ω undergoes significant oscillations. In general, more negative values of Γ_3/ω represent a vortex closer to nonlinear resonance meaning that on the phase-plane representation the loop of the separatrix shrinks (Fig. 5, right panel). In fact, if the rotational component exceeds (i.e. is more negative than) a critical value Ω_c, which is ~ -0.168 when the strain components are kept at the value $(-0.0233, -0.0237)$, the loop of the separatrix as well as the nutating regime disappears, and the vortex enters a high-ellipticity oscillation regime, manifesting in a vortex split. However, it can be shown that if the strain magnitude decreases, the critical value Ω_c becomes more negative and therefore stronger rotational component is necessary to trigger a vortex split. Consequently, in order to characterise the likelihood of vortex splits on Mars, the relationship between strain and rotation should be also considered.

We calculate the correlation coefficient between the strain magnitude and the magnitude of the rotational component for Martian Years 24–26, 30–32 separately, and we find that

$$corr(|\boldsymbol{\Gamma}_H|/\omega, |\Gamma_3|/\omega) = -0.74, -0.63, -0.58, -0.85, -0.69, -0.59 \quad (12)$$

in Martian Years 24–26, 30–32 respectively, a relatively strong negative correlation in each of the six years. The correlation suggests that a stronger (more negative) rotational component tends to be accompanied with a weaker strain. This relationship is possibly a key feature

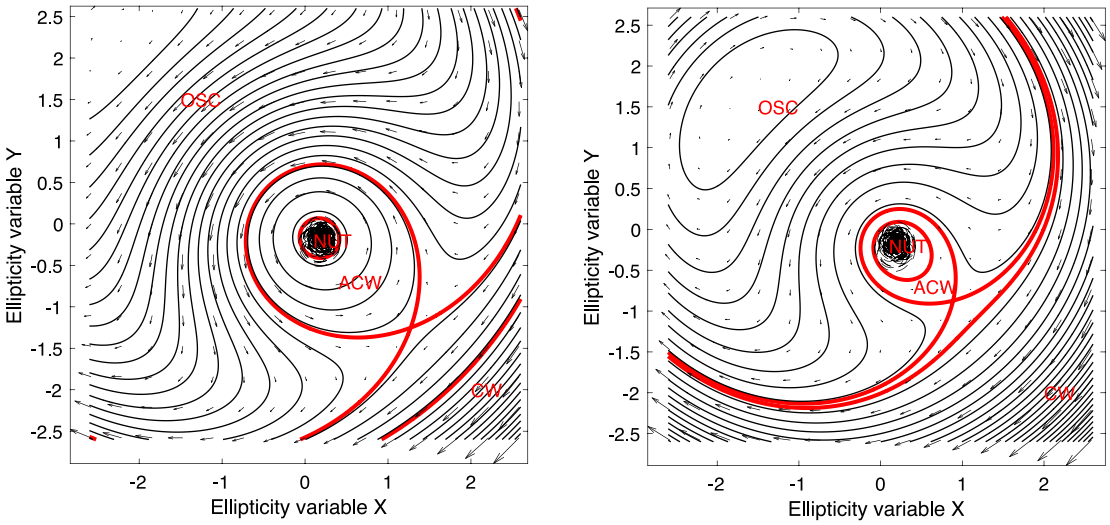


Fig. 5. The structure of the Hamiltonian orbits for strain-rotation vector $\boldsymbol{\Gamma}/\omega = (-0.0233, -0.0237, -0.1031)^T$ (left panel), which is the stationary part of the background flow between $L_s = 240° - 330°$ in MYs 24–26, and $\boldsymbol{\Gamma}/\omega = (-0.0233, -0.0237, -0.14)^T$ (right panel), which is associated to a typical background flow when the surf zone parameter is large (more negative). Both figures, the red contour through the origin represents the boundary between a nutating (NUT) and an anticlockwise (ACW) regime. A second red contour, the separatrix, separates the ACW and oscillating (OSC) regimes. The evolution of the assimilated ellipticity vector is also shown for the $L_s = 240° - 330°$ interval in MY 24, filling the entire nutating regime on the left panel. Arrows are proportional to $\nabla^{\perp} H$, visualising the direction (and intensity) of the oscillations. (For interpretation of the references to colour in this figure legend, the reader is referred to the web version of this article.)

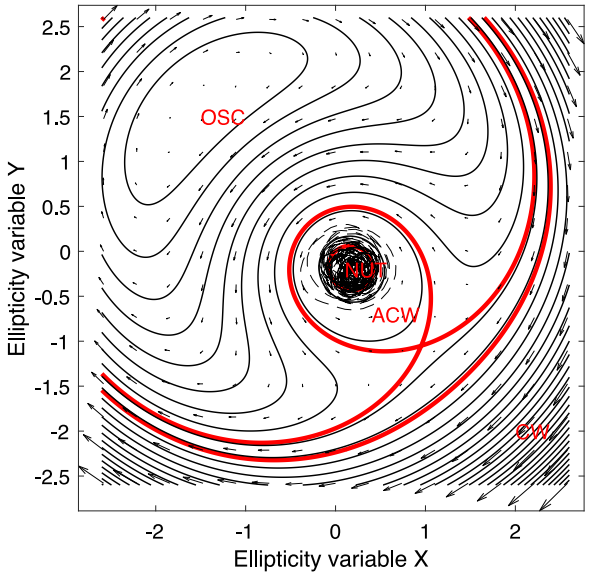


Fig. 6. The structure of the Hamiltonian orbits for strain-rotation vector $\boldsymbol{\Gamma}/\omega = (-0.0193, -0.0175, -0.1363)^T$, which is the stationary part of the background flow between $L_s = 240° - 330°$ in MYs 30–32. As on Fig. 5, the red contour through the origin represents the boundary between a nutating (NUT) and an anticlockwise (ACW) regime. A second red contour, the separatrix, separates the ACW and oscillating (OSC) regimes. The evolution of the assimilated ellipticity vector is also shown for the $L_s = 240° - 330°$ interval in MY 30, showing that the vortex evolution undergoes both NUT- and ACW-type oscillations. (For interpretation of the references to colour in this figure legend, the reader is referred to the web version of this article.)

that acts against high amplitude vortex events on Mars. Vortex splits require both a strain and a rotational component that is stronger than their climatological value (based on six Martian Years of reanalysis data). However the strength of the strain and the rotational component are strongly and negatively correlated, suggesting that a simultaneous increase in both – i.e. vortex splits on Mars – are statistically rare events.

3.3. Interpretation of the strain component

3.3.1. Wavenumber-2 topography on the Martian northern hemisphere

In this section, we discuss the contribution of topography to the stationary component of the strain vector. Our topographic data is derived from the Mars MGS MOLA Elevation Model 463 m (MEGDR) on a 0.25° × 0.25° grid and the spherical structure is mapped on a plane by using Lambert's area-preserving projection. Working in polar coordinates, the topography $\iota(r, \theta)$ can be expressed as a Fourier-series

$$\iota(r, \theta) = A_0(r) + \sum_{m=1}^{\infty} \left(A_m(r) \cos m\theta + B_m(r) \sin m\theta \right), \tag{13}$$

where the coefficients $A_2(r)$, $B_2(r)$ are determined by using the standard techniques of Fourier analysis. The amplitude $h(r)$ and phase $\phi(r)$ of the wavenumber-2 component ι_2 are simply given by

$$\begin{aligned} h(r) &= \sqrt{A_2(r)^2 + B_2(r)^2}, \\ \phi(r) &= \frac{1}{2} \tan^{-1} \frac{B_2(r)}{A_2(r)}, \end{aligned} \tag{14}$$

so that

$$\iota_2(r, \theta) = A_2(r) \cos 2\theta + B_2(r) \sin 2\theta = h(r) \cos 2(\theta - \phi_2(r)), \tag{15}$$

and are shown on Figs. 7 and 8, respectively. The phase of the wavenumber-2 component varies little with latitude, staying close to the 67° longitude circle. Therefore, we keep $\phi_2(r) = \phi_0 = 1.1705$ in radians for simplicity (which corresponds to the 67° longitude circle). Now, we write $h(r)$ as a Fourier–Bessel series

$$h(r) = \sum_{n=1}^{\infty} d_n J_2(u_n \frac{r}{b}), \tag{16}$$

where J_2 is the Bessel-function of the first kind, u_n are the positive zeros of J_2 and b is the distance between the pole and the equator under Lambert's projection. The coefficients d_n are determined from the orthogonality condition and are given by

$$d_n = \frac{\int_0^b r h(r) J_2(u_n \frac{r}{b}) \mathrm{d}r}{\frac{1}{2}(b J_1(u_n))^2}. \tag{17}$$

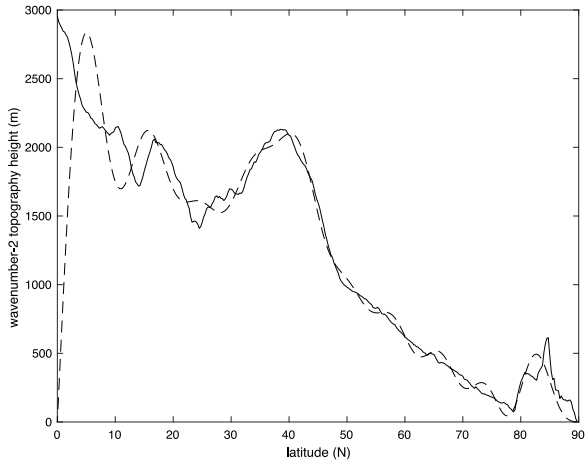


Fig. 7. Amplitude of the wavenumber-2 topography (solid) and its Fourier–Bessel approximation truncated at the 20th zero.

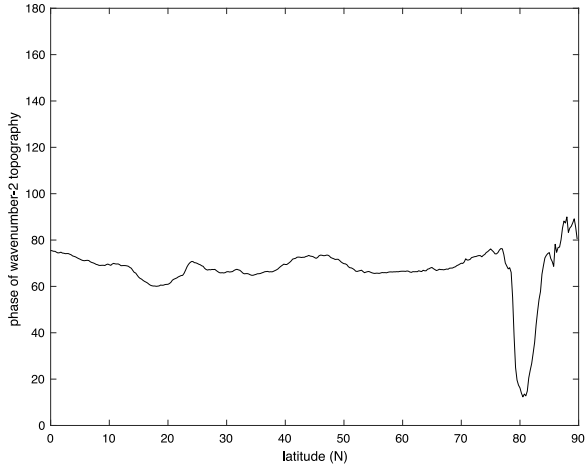


Fig. 8. Phase of the wavenumber-2 component of the topography.

The Fourier–Bessel series obtained after truncating at u_{20} is shown on Fig. 7 and agrees quite well with the full wavenumber-2 topography everywhere apart from the equatorial regions (which is expected as, by construction, the Fourier–Bessel series is zero at $r = b$).

3.3.2. Characterisation of the topography-induced strain

In this section, we aim to characterise the effective wavenumber-2 topographic forcing and its manifestation as a strain in a single-layer shallow water f-plane model. Both modelling and observational studies (Haberle et al., 2020; Hollingsworth and Barnes, 1996) show that the phase of the topographic wavenumber-2 wave does not vary significantly in the vertical direction and the wave can propagate up high in the atmosphere (depending on atmospheric conditions, such as dustiness), and the wave forcing is in general strongest at $\sim 35-40$ km altitudes (which is approximately at the 350 K potential temperature level at polar regions). We should also note that this level is almost four times the Martian scale height (approximately 10.8 km). Consequently, while the amplitude of the effective wavenumber-2 topographic forcing experienced by the vortex cannot be directly compared to the wavenumber-2 component ι_2 of the topography, the phase varies little with height and one may assume that the time-dependent effective wavenumber-2 forcing takes the form

$$\Xi(r,\theta,t) = M(r,t)\cos 2(\theta-\phi_0), \tag{18}$$

where the magnitude of the forcing is given by a Fourier–Bessel series

$$M(r,t) = \sum_{n=1}^{\infty} c_n(t) d_n J_2(u_n \frac{r}{b}), \tag{19}$$

where the unsteady amplitudes $c_n(t)$ of the different modes depend on the atmospheric conditions for wave-propagation and describe the effective strength of the different modes at vortex level. In particular, dusty conditions are associated to suppressed vertical wave-propagation (Barnes and Hollingsworth, 1987) and may result in lower values of the wave amplitudes $c_n(t)$.

In a single-layer shallow water f-plane model it is possible to replace the topographic forcing by a topographic streamfunction (Matthewman and Esler, 2011) so that the new system does not have a topography, but an additional streamfunction is included, resulting in the same dynamics. The topographic streamfunction associated to Ξ is given by

$$\psi = \frac{f_0}{H}\sum_{n=1}^{\infty} c_n(t) d_n \frac{J_2\left(u_n \frac{r}{b}\right)\cos 2(\theta-\phi_0)}{\left(\frac{u_n}{b}\right)^2 + L_R^{-2}}, \tag{20}$$

where H is the mean depth of the layer, f_0 is the Coriolis parameter at the pole and $L_R = 1800$ km is the Rossby deformation radius. Next, following Matthewman and Esler (2011), we use the approximation

$$J_2(\lambda r) \sim \frac{J_2(\lambda R)}{R^2} r^2 \tag{21}$$

to approximate the strain field experienced at the vortex edge, where the value of $R = 1662$ km can be chosen as a typical value for the vortex radius (under Lambert's projection — which is not distance-preserving), to find

$$\psi = \frac{f_0}{H} r^2 \cos 2(\theta-\phi_0) C := \frac{f_0}{H} r^2 \cos 2(\theta-\phi_0) \sum_{n=1}^{\infty} c_n(t) d_n \frac{J_2(u_n \frac{R}{b})}{\left(\frac{u_n R}{b}\right)^2 + \left(\frac{R}{L_R}\right)^2}. \tag{22}$$

By introducing $(x,y) = r(\cos(\theta-\phi_0-\pi/4), \sin(\theta-\phi_0-\pi/4))$, the streamfunction takes the form of a simple strain flow

$$\psi = -\Gamma(t) x y, \tag{23}$$

with $\Gamma(t) = 2C(t)\frac{f_0}{H}$, where

$$C(t) = \sum_{n=1}^{\infty} c_n(t) d_n \frac{J_2(u_n \frac{R}{b})}{\left(\frac{u_n R}{b}\right)^2 + \left(\frac{R}{L_R}\right)^2} := \sum_{n=1}^{\infty} c_n(t) F_n, \tag{24}$$

showing that the strain strength $\Gamma(t)$ can be expressed as a weighted sum of the amplitudes of the wave modes $c_n(t)$, leading to a weaker strain flow when the wave amplitudes are suppressed. Here, one should note that the constants F_n are determined completely by the Martian topography and the typical value of the vortex radius.

It is useful to compare the direction of the strain axis resulting from topographic forcing to the stationary component of the strain revealed by the dynamical elliptical diagnostics method. The formulation of the (x,y) coordinates show that the topographic forcing induced strain has its principal x-axis aligned at

$$\Phi = \phi_0 + 45° \sim 112° \tag{25}$$

in the original frame of reference, since in (x,y)-coordinates, the principal axis of a strain flow with streamfunction $\phi = -\Gamma xy$ is the x-axis, and $x = r\cos(\theta-\phi_0-\pi/4)$ in the original, topography based frame of reference. On the other hand, the output of the dynamical elliptical diagnostics describe a strain flow with a stationary component that takes the value $(\Gamma_1,\Gamma_2)/\omega = (-0.0233, -0.0237)$ during the winter periods in MYs 24–26 and $(\Gamma_1,\Gamma_2)/\omega = (-0.0193, -0.0175)$ during MYs 30–32. We can rewrite the stationary component in amplitude-phase form $(\Gamma_1,\Gamma_2)/\omega = |\Gamma|(\cos 2\Phi_{st}, \sin 2\Phi_{st})/\omega$, leading to

$$\Phi_{st} = \frac{1}{2}\tan^{-1}(-0.0237/-0.0233) \sim 112.74° \tag{26}$$

in MYs 24–26, and

$$\Phi_{st} = \frac{1}{2}\tan^{-1}(-0.0175/-0.0193) \sim 111.90° \quad (27)$$

in MYs 30–32. The agreement between the phase Φ of the topography induced strain, and the phase Φ_{st} of the stationary component of the assimilated strain strongly supports that the stationary component of the wavenumber-2 forcing experienced by the vortex is induced by Martian topography. However, the strength of the strain experienced by the vortex depends on the amplitudes $c_n(t)$ that can be suppressed or enhanced depending on different atmospheric conditions, e.g. dust loading, hence the wave amplitudes cannot be directly compared to the topography itself.

3.4. Interpretation of the rotation component

The rotational component of the strain-rotation vector is commonly referred to as a 'surf zone parameter' in studies modelling stratospheric polar vortices on Earth (e.g. Matthewman and Esler, 2011), and is interpreted as a parameter controlling the strength of the stratospheric jet outside the vortex. While Mars has no stratosphere, and one should not call the upper part of the Martian Hadley cell a surf zone, the rotational component is still a descriptor of the subpolar wind and PV structure. A straightforward translation of the interpretation to Mars is by seeing Γ_3/ω as a descriptor of the strength of the zonal mean zonal wind structure in the Hadley cell, compared to the strength of the polar vortex jet. A useful way of seeing how the strength of this single parameter manifests is to compare the time mean of the zonal wind field during high Γ_3 events with climatological winds (Fig. 9). Here, we use $\Omega_c = -0.12$ to distinguish between high rotation ($\Gamma_3/\omega < \Omega_c$) events and climatology in MYs 24–26. It is revealed clearly, that during these events the strength of the polar vortex jet is characteristically weaker (less positive) as are the zonal mean zonal winds in the Hadley cell (less negative). On the opposite hemisphere, there is a very strong strengthening at midlatitudes at all heights. In contrast, when we apply the same analysis for MYs 30–32, we find no significant difference between high rotation events and climatology (Fig. 10). While the difference of the high rotation and climatological zonal winds is in the range $(-10,20)$ ms^{-1} in MYs 24–26, we find that this range becomes $(-2,2)$ ms^{-1} at the Northern Hemisphere in MYs 30–32 (if we disregard the uppermost levels of the reanalysis). Therefore, we cannot find any clear signal of the rotational component in the zonal wind structure in MYs 30–32. It is possible that this is a consequence of the qualitatively different evolution of the rotational component in the MYs 24–26 and the MYs 30–32 period. While most of the high-rotation events are consistently appear late-winter in MYs 24–26, the rotational component was more negative for a prolonged period in MYs 30–32. In order to investigate the impact of the rotational component, we now restrict our attention to MYs 24–26.

It is also useful to consider the relation between the rotational component of the assimilated background flow and the zonal wind structure. Next, we calculate the correlation coefficient of the rotational component Γ_3/ω and the zonal mean zonal wind at any given latitude and height and a contour plot of the correlation coefficient is shown on Fig. 11 for MYs 24–26. There are two regions of particularly high correlation. Inside the polar vortex itself, a typical correlation coefficient that is larger than 0.4 is present throughout, meaning that a more negative (and so stronger) rotational component is in general accompanied with a less positive (i.e. weaker) polar jet. On the other hand, the majority of the Hadley cell is characterised by a correlation coefficient that is more negative than −0.4, suggesting that a more negative rotational component is in general corresponds to a less negative (i.e. weaker easterly) zonal mean zonal wind.

The trends revealed by the correlation coefficients analysis and the zonal mean zonal wind anomaly (Fig. 9) both support the notion that the rotational component of the strain-rotation vector is a descriptor of the strength of the winds in the Hadley cell, relative to the strength of the polar vortex jet.

The role of high Γ_3/ω events can be further elucidated if we compare the magnitude of the ellipticity vector (Fig. 12) with the rotational component. It is interesting to see that both high and small ellipticity become more frequent when the rotational component becomes more negative. These results are supported by studies of nonlinear resonant excitation of polar vortices on Earth (Esler and Mester, 2019; Matthewman and Esler, 2011; Plumb, 1981), namely, vortex states closer to linear resonance ($\Gamma_3/\omega = -0.25$) may exhibit higher ellipticity oscillations. However, in the case of the Martian NH polar vortex, high aspect ratios are not necessarily a result of near-resonant nonlinear behaviour of the vortex. Rather, high (more negative) rotational components correspond to an enlarged NUT regime where larger ellipticity nutations and thus higher aspect ratios are available.

4. Conclusions

We have applied the dynamical elliptical diagnostics on the evolution of the Martian Northern Hemisphere polar vortex during the winter seasons ($L_s = 240° - 330°$) of Martian Years 24–26 and 30–32. Despite the limitations of the applied modelling approach, it complements the recent developments (Ball et al., 2021; Scott et al., 2020; Streeter et al., 2021) on the role of topographic forcing and the dusty Hadley cell in the formation and variability of the Martian polar vortex well, by providing a new, dynamical perspective on how the topographic forcing and the Hadley cell drive the vortex and why vortex splits are rare events on Mars.

The outcome of the analysis is an assimilated background flow, consisting of a strain field and a background rotation most consistent with the evolution of the (outer) edge of the vortex. The stationary part of the strain field is linked to waves generated by Martian topography, and the rotational component is interpreted as a descriptor of the strength of the Hadley cell winds. Using this interpretation of the evolution of the strain on Fig. 3, our results suggests that there was a high wavenumber-2 topographic wave activity during the 240-290°Ls period in MYs 24–26 and the 290-320°Ls period in MYs 30–32.

There is a large variability in the rotational component, and it is (negatively) correlated with the strength of the topographic forcing. The typical value of the strain-rotation vector results in a vortex that undergoes a small amplitude, nutating motion in MYs 24–26, and undergoes both nutating motion and small amplitude, anticlockwise motion in MYs 30–32. In MYs 24–26, the typical strength of the strain relative to the vortex ($|\boldsymbol{\Gamma}_{H,m}|/\omega \sim 0.0332$) is strong enough to explain the vortex nutating around a fixed orientation with the unsteady component $\boldsymbol{\Gamma}_H - \boldsymbol{\Gamma}_{H,m}$ being weaker than the mean and not having a strongly preferred direction. This is in contrast with the strain vector relevant to the Southern Hemisphere stratospheric polar vortex on Earth, where the mean is dominated by the unsteady component (Mester and Esler, 2020). However, decomposing the strain component into a sum of a stationary and an unsteady part may not be physically meaningful, as the effects of the stationary (topographic) forcing and non-stationary forcing (e.g. thermal) may not add up linearly, as suggested by the strong negative correlation with the rotational component, representing the strength of the zonal mean zonal winds in the Hadley cell. Phase-portrait representations (see Fig. 5) show that the lack of high amplitude events can be explained by the relatively low value of Γ_3/ω and its strong negative correlation with the strain magnitude. High amplitude vortex events require both a rotational component that is much more negative than its climatological value and a strain component that is larger in magnitude than its climatological value. However, the strain and rotational components are shown to be strongly negatively correlated, suggesting that it is statistically rare that both components would attain high values, and that vortex splitting on Mars is a rare event.

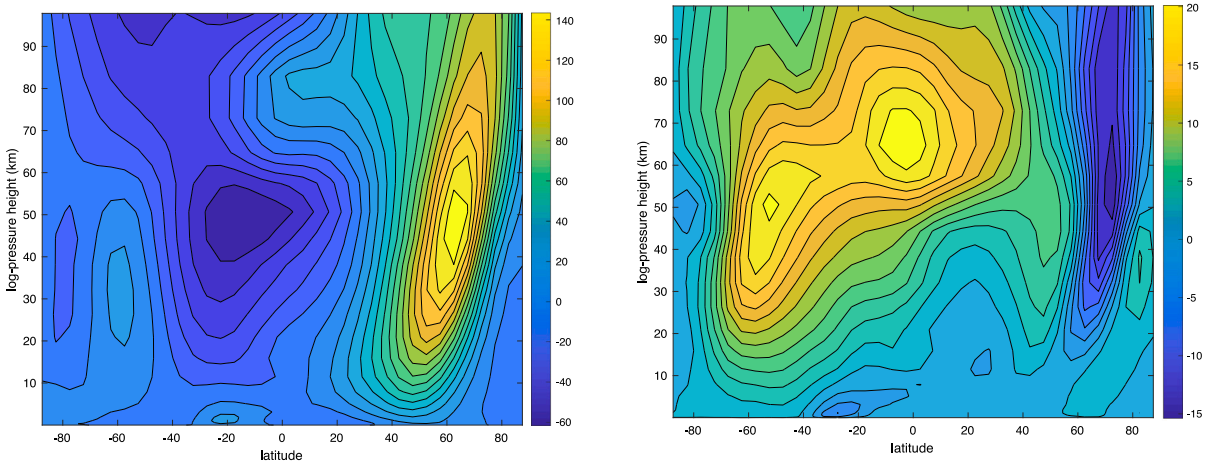


Fig. 9. The time-averaged zonal wind (units are in m/s) during $\Gamma_3/\omega < -0.12$ events between $L_s = 240° - 330°$ in MYs 24–26 (left) and the anomaly compared to the climatological zonal winds during $L_s = 240° - 330°$ in MYs 24–26 (right).

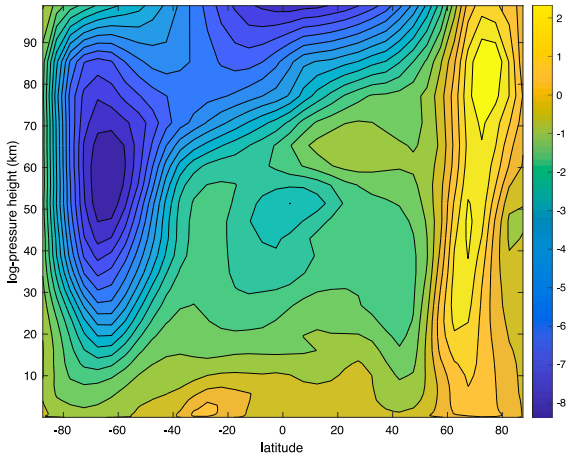


Fig. 10. The anomaly in the time-averaged zonal wind (units are in m/s) during $\Gamma_3/\omega < -0.12$ events compared to the climatological zonal winds during $L_s = 240° - 330°$ in MYs 30–32.

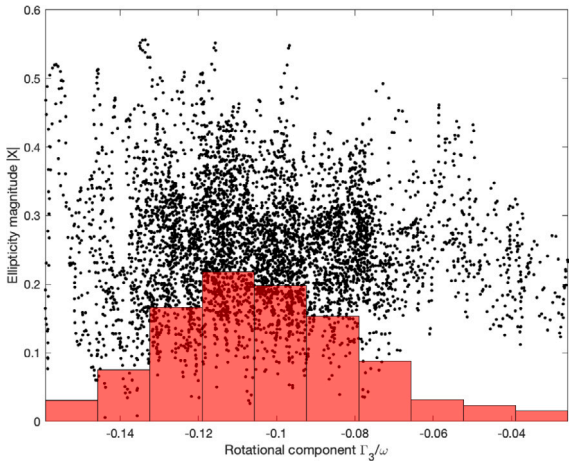


Fig. 12. Scatterplot showing the magnitude of the ellipticity vector and the rotational component every 2 h during $L_s = 240° - 330°$ in MYs 24–26. The histogram shows the number of data points with respect to the rotational component.

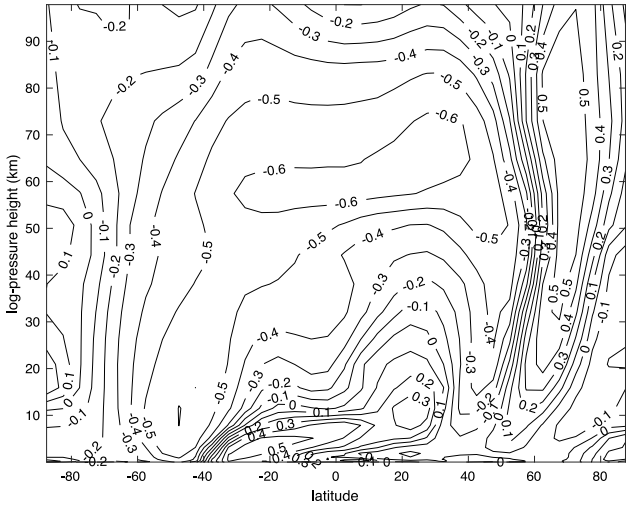


Fig. 11. The correlation between the rotational component at the 350 K isentropic level and the zonal mean zonal wind structure between $L_s = 240° - 330°$ in MYs 24–26.

By comparing the evolution of the Martian NH polar vortex to stratospheric polar vortices on Earth using the perspective of Kida's model, we find that the typical (or mean) conditions occupy a qualitatively different place on the $(|\boldsymbol{\Gamma_H}/\omega|, \Gamma_3/\omega)$ parameter space, corresponding to qualitatively different regimes of behaviour (NUT for the Martian NH polar vortex and ACW for stratospheric polar vortices on Earth).

In a wider context, it could be insightful to consider how planetary-scale planetary vortices (that can be characterised as a region of elevated PV and a sufficiently near-elliptical shape) are controlled by their strain-rotation vectors and how similarities and differences between two vortices can be explained by the location of their characteristic strain-rotation vector in the $(|\boldsymbol{\Gamma_H}/\omega|, \Gamma_3/\omega)$ parameter space. This could include the topic of filamentation, since the instability analysis of Kida's vortices (Dritschel, 1990) suggests that the extent of vortex filamentation is regime behaviour, arguing that in the ACW regime modes on the vortex edge are characterised by higher growth rates than modes on the edge of a vortex in the NUT regime. Therefore it is possible that the lack of filamentation of the Martian NH polar vortex observed in reanalysis data is not an artefact of the resolution, but a result of regime behaviour (i.e. it depends on which regime, NUT or ACW, the vortex is located at) and is a feature typical of nutating vortices, suggesting that future research regarding filamentation of the Martian Northern Hemisphere polar vortex could consider the role of nutating vortex regimes. While a consistent correlation between the

rotational and strain components has been revealed by our analysis, our study is lacking a physical explanation of this interaction. It is possible, that high topographic forcing events suggest low dust spells, and in return a weaker Hadley-cell. For future research, the likelihood and effect of vortex splits could be also considered in idealised model studies. While our results suggest that they are rare events on Mars, the occurrence of a vortex split would change the large-scale circulation and atmospheric transport, affecting dust and water cycles as well as trace gas distributions.

Acknowledgements

The author would like to thank Darryn Waugh, Richard Scott, Ted Johnson, Gavin Esler and two anonymous reviewers for their useful comments on the early version of the manuscript. The MACDA MGS/TES v1.0 dataset is publicly available from Montabone et al. (2011) and the OpenMARS dataset is available from Holmes et al. (2019). This research was funded by EPSRC, United Kingdom Studentship Award 1777889.

Appendix A. Construction of the elliptical diagnostics

Lambert's azimuthal equal-area projection is used to map the spherical geometry on a plane, $(\lambda, \phi) \to (x, y) = R\sqrt{2(1-\sin\phi)}(\cos\lambda, \sin\lambda)$, where λ is the longitude, ϕ is the latitude and R is the radius of Mars, to map the vortex boundary and the PV structure of the Northern Hemisphere to a plane from spherical geometry. To define the vortex boundary, we average the potential vorticity polewards of 32.5°, and we take the contour corresponding to this average value $q_b(\theta, t)$ on the θ potential temperature level. The averaged potential vorticity that defines the polar vortex edge is chosen so that the relatively low values around the pole are still higher, meaning that the resulting vortex remains simply-connected. Note that this is a different definition from Mitchell et al. (2015), where the vortex boundary was defined by the equivalent latitude where the potential vorticity gradient is the largest. The application of such definition on the time-averaged vortex results in an annular vortex fit. Without doubt, this method could also act as a good way to describe the elliptical nature of the vortex, however, it might provide a more realistic fit if the whole region is considered within a simply-connected domain. Next, the potential vorticity field is modified according to

$$\hat{q}(\mathbf{x}, \theta, t) = \begin{cases} q(\mathbf{x}, \theta, t), & q(\mathbf{x}, \theta, t) > q_b(\theta, t) \\ q_b(\theta, t) & q(\mathbf{x}, \theta, t) \le q_b(\theta, t), \end{cases} \tag{28}$$

i.e. low latitude PV variations are neglected by setting the PV to be constant outside the vortex, and the $M_{k,l}(\theta, t)$ moment diagnostic is defined by the area integral

$$M_{k,l} = \int_{\mathbb{R}^2} (\hat{q}(x, y) - q_b) x^k y^l \, \mathrm{d}x \, \mathrm{d}y. \tag{29}$$

Note that the integrand vanishes outside of the vortex. Following Matthewman et al. (2009), the equivalent ellipse is defined to have a constant uniform interior PV ($q_c + q_b$, where the value of q_c determines the area of the equivalent ellipse, not shown here), and is otherwise chosen to match the zeroth, first and second-order moments of the observed vortex. First, the centre of the equivalent ellipse is given by

$$(\bar{x}, \bar{y}) = \frac{1}{M_{0,0}} (M_{1,0}, M_{0,1}), \tag{30}$$

and the relative vortex moments are defined to be

$$J_{k,l} = \int_{\mathbb{R}^2} (\hat{q}(x, y) - q_b)(x - \bar{x})^k (y - \bar{y})^l \mathrm{d}x \, \mathrm{d}y. \tag{31}$$

Now, the orientation Θ, and the aspect ratio Λ of the equivalent ellipse are given by the formulae

$$\begin{aligned} \Theta &= \frac{1}{2} \tan^{-1}\Big(\frac{2J_{1,1}}{J_{2,0} - J_{0,2}} \Big), \\ \Lambda &= \left| \frac{J_{2,0} + J_{0,2} + \sqrt{4J_{1,1}^2 + (J_{2,0} - J_{0,2})^2}}{J_{2,0} + J_{0,2} - \sqrt{4J_{1,1}^2 + (J_{2,0} - J_{0,2})^2}} \right|^{1/2}. \end{aligned} \tag{32}$$

Appendix B. Solution of the optimisation problem

The minimiser functions of the functional J are obtained by solving the Euler–Lagrange equations,

$$\begin{aligned} \dot{\boldsymbol{\Gamma}} &= -\tfrac{1}{2}(\nabla_{\boldsymbol{\Gamma}} \boldsymbol{F}) \cdot \boldsymbol{\mu}, \\ \dot{\boldsymbol{\mu}} &= 2\epsilon^2 (\boldsymbol{X} - \boldsymbol{X}_{\boldsymbol{obs}}) - (\nabla \boldsymbol{F}) \cdot \boldsymbol{\mu}, \\ \dot{\boldsymbol{X}} &= \boldsymbol{F}. \end{aligned} \tag{33}$$

where $\nabla_{\boldsymbol{\Gamma}} = (\partial_{\Gamma_1}, \partial_{\Gamma_2}, \partial_{\Gamma_3})^T$ is the gradient operator in the space of the vector $\boldsymbol{\Gamma}$ and $\nabla_{\boldsymbol{\Gamma}} \boldsymbol{F}$ denotes the 3×2 matrix with components $\partial_{\Gamma_i} F_j$. The boundary conditions are given by

$$\begin{aligned} \dot{\boldsymbol{\Gamma}}(0) &= \dot{\boldsymbol{\Gamma}}(T) = 0 \\ \boldsymbol{\mu}(0) &= \boldsymbol{\mu}(T) = 0. \end{aligned} \tag{34}$$

The system (33)–(34) is solved numerically using a generalisation of the shooting method. The numerical implementation is discussed in Mester and Esler (2020) in more detail, and a code, written in MATLAB, is available from the author of this article upon request.

References

Ball, E.R., Mitchell, D.M., Seviour, W.J.M., Thomson, S.I., Vallis, G.K., 2021. The roles of latent heating and dust in the structure and variability of the northern martian polar vortex. Planet. Sci. 2 (203), http://dx.doi.org/10.3847/psj/ac1ba2.

Barnes, J.R., Haberle, R.M., 1996. The martian zonal-mean circulation: Angular momentum and potential vorticity structure in gcm simulations. J. Atmos. Sci. 53, 3143–3156. http://dx.doi.org/10.1175/1520-0469(1996)053<3143:TMZMCA>2.0.CO;2.

Barnes, J.R., Hollingsworth, J.L., 1987. Dynamical modeling of a planetary wave mechanism for a martian polar warming. Icarus 71, 313–334. http://dx.doi.org/10.1016/0019-1035(87)90156-4.

Dritschel, D.G., 1990. The stability of elliptical vortices in an external straining flow. J. Fluid Mech. 210, 223–261.

Esler, J.G., Mester, M., 2019. Noise-induced vortex splitting stratospheric sudden warmings. Q. J. R. Meteorol. Soc. 145, 476–494.

Greybush, S.J., Gillespie, H.E., Wilson, R.J., 2019. Transient eddies in the tes/mcs ensemble mars atmosphere reanalysis system (emars). Icarus 317, 158–181. http://dx.doi.org/10.1016/j.icarus.2018.07.001, URL: https://www.sciencedirect.com/science/article/pii/S001910351730756X.

Guzewich, S.D., Toigo, A., Waugh, D., 2016. The effect of dust on the martian polar vortices. Icarus 278, 100–118. http://dx.doi.org/10.1016/j.icarus.2016.06.009.

Haberle, R.M., Kahre, M.A., Barnes, J.R., Hollingsworth, J.L., Wolff, M.J., 2020. Marci observations of a wavenumber-2 large-scale feature in the north polar hood of mars: Interpretation with the nasa/ames legacy global climate model. Icarus 335, 113367. http://dx.doi.org/10.1016/j.icarus.2019.07.001.

Hollingsworth, J.L., Barnes, J.R., 1996. Forced stationary planetary waves in Mars's winter atmosphere. J. Atmos. Sci. 53, 428–448. http://dx.doi.org/10.1175/1520-0469(1996)053<0428:FSPWIM>2.0.CO;2.

Holmes, J., Lewis, S., Patel, M., 2019. Openmars Database. http://dx.doi.org/10.21954/ou.rd.c.4278950.

Holton, J.R., Mass, C., 1976. Stratospheric vacillation cycles. J. Atmos. Sci. 33, 2218–2225.

Kida, S., 1981. Motion of an elliptic vortex in a uniform shear flow. J. Phys. Soc. Japan 50, 3517–3520.

Matthewman, N.J., Esler, J.G., 2011. Stratospheric sudden warmings as self-tuning resonances. Part I: vortex splitting events. J. Atmos. Sci 68, 2481–2504.

Matthewman, N.J., Esler, J.G., Charlton-Perez, A.J., Polvani, L.M., 2009. A new look at stratospheric sudden warmings. Part III. Polar vortex evolution and vertical structure. J. Clim. 22, 1566–1585.

Melander, M.V., Zabusky, N.J., Styczek, A.S., 1986. A moment model for vortex interactions of the two-dimensional Euler equations. Part 1. Computational validation of a Hamiltonian elliptical representation. J. Fluid Mech. 167, 95–115.

Mester, M., Esler, J.G., 2020. Dynamical elliptical diagnostics of the antarctic polar vortex. J. Atmos. Sci. 77, 1167–1180. http://dx.doi.org/10.1175/JAS-D-19-0232.1.

Mitchell, D., Montabone, L., Thomson, S., Read, P., 2015. Polar vortices on earth and mars: A comparative study of the climatology and variability from reanalyses. Q. J. R. Meteorol. Soc. 141, 550–562.

Montabone, L., Lewis, S., Read, P., 2011. Mars Analysis Correction Data Assimilation (Macda): Mgs/Tes V1.0. NCAS British Atmospheric Data Centre, http://dx.doi.org/10.5285/78114093-E2BD-4601-8AE5-3551E62AEF2B.

Montabone, L., Marsh, K., Lewis, S.R., Read, P.L., Smith, M.D., Holmes, J., Spiga, A., Lowe, D., Pamment, A., 2014. The mars analysis correction data assimilation (macda) dataset v1.0. Geosci. Data J. 1, 129–139. http://dx.doi.org/10.1002/gdj3.13.

Plumb, R.A., 1981. Instability of the distorted polar night vortex: A theory of stratospheric warmings. J. Atmos. Sci. 38, 2514–2531.

Rostami, M., Zeitlin, V., Montabone, L., 2018. On the role of spatially inhomogeneous diabatic effects upon the evolution of mars' annular polar vortex. Icarus 314, 376–388. http://dx.doi.org/10.1016/j.icarus.2018.05.026.

Scott, R.K., Seviour, W.J.M., Waugh, D.W., 2020. Forcing of the martian polar annulus by hadley cell transport and latent heating. Q. J. R. Meteorol. Soc. 146, 2174–2190. http://dx.doi.org/10.1002/qj.3786.

Seviour, W., Waugh, D., Scott, R., 2017. The stability of mars's annular polar vortex. J. Atmos. Sci. 74, 1533–1547. http://dx.doi.org/10.1175/JAS-D-16-0293.1.

Smith, M.D., 2004. Interannual variability in tes atmospheric observations of mars during 1999–2003. Icarus 167, 148–165. http://dx.doi.org/10.1016/j.icarus.2003.09.010, special Issue on DS1/Comet Borrelly.

Streeter, P.M., Lewis, S.R., Patel, M.R., Holmes, J.A., Fedorova, A.A., Kass, D.M., Kleinböhl, A., 2021. Asymmetric impacts on mars' polar vortices from an equinoctial global dust storm. J. Geophys. Res.: Planets 126, e2020JE006774. http://dx.doi.org/10.1029/2020JE006774.

Toigo, A.D., Waugh, D.W., Guzewich, S.D., 2017. What causes mars' annular polar vortices? Geophys. Res. Lett. 44, 71–78. http://dx.doi.org/10.1002/2016GL071857.

Waugh, D.W., 1997. Elliptical diagnostics of stratospheric polar vortices. Q. J. R. Meteorol. Soc. 123, 1725–1748.

Waugh, D.W., Toigo, A.D., Guzewich, S.D., Greybush, S.J., Wilson, R.J., Montabone, L., 2016. Martian polar vortices: Comparison of reanalyses. J. Geophys. Res.: Planets 121, 1770–1785. http://dx.doi.org/10.1002/2016JE005093.

Wilson, R.J., 1997. A general circulation model simulation of the martian polar warming. Geophys. Res. Lett. 24, 123–126. http://dx.doi.org/10.1029/96GL03814.